How the growth of ice depends on the fluid dynamics underneath

Ziqi Wang[a], Enrico Calzavarini[b], Chao Sun[a,c,1], and Federico Toschi[d,e]

[a]Center for Combustion Energy, Key Laboratory for Thermal Science and Power Engineering of Ministry of Education, Department of Energy and Power Engineering, Tsinghua University, 100084 Beijing, China; [b]Unité de Mécanique de Lille–J. Boussinesq, Unité Labellisée de Recherche 7512, Université Lille, F-59000 Lille, France; [c]Department of Engineering Mechanics, School of Aerospace Engineering, Tsinghua University, Beijing 100084, China; [d]Department of Applied Physics, Eindhoven University of Technology, 5600 MB Eindhoven, The Netherlands; and [e]Istituto per le Applicazioni del Calcolo "M. Picone"–Consiglio Nazionale delle Ricerche, I-00185 Rome, Italy

Convective flows coupled with solidification or melting in water bodies play a major role in shaping geophysical landscapes. Particularly in relation to the global climate warming scenario, it is essential to be able to accurately quantify how water-body environments dynamically interplay with ice formation or melting process. Previous studies have revealed the complex nature of the icing process, but have often ignored one of the most remarkable particularities of water, its density anomaly, and the induced stratification layers interacting and coupling in a complex way in the presence of turbulence. By combining experiments, numerical simulations, and theoretical modeling, we investigate solidification of freshwater, properly considering phase transition, water density anomaly, and real physical properties of ice and water phases, which we show to be essential for correctly predicting the different qualitative and quantitative behaviors. We identify, with increasing thermal driving, four distinct flow-dynamics regimes, where different levels of coupling among ice front and stably and unstably stratified water layers occur. Despite the complex interaction between the ice front and fluid motions, remarkably, the average ice thickness and growth rate can be well captured with the theoretical model. It is revealed that the thermal driving has major effects on the temporal evolution of the global icing process, which can vary from a few days to a few hours in the current parameter regime. Our model can be applied to general situations where the icing dynamics occur under different thermal and geometrical conditions.

Rayleigh–Bénard convection | solidification | density anomaly | hydrodynamic turbulence | ice dynamics

Many geophysical patterns result from the interaction between fluid motions and the dynamical evolution of solid-phase boundaries. Usually, the dynamics of the solid boundaries are due to phase change or erosion. Examples range from sculpting of the glacier, ice shelf, iceberg, and sea caves due to flows in the oceans to congelation ice forming in ponds and lakes and many geological patterns (1) and astrophysical landforms (2), as well as in our daily lives and many industrial processes (3, 4).

Generally, warm water (freshwater or water with low enough salinity) is lighter and so it floats, whereas cold water is denser and therefore it sinks. However, this is not the case once water is around the density-peak temperature, T_c (around $4\ ^\circ$C), when its density reaches the maximum: Water expands when it is colder than T_c (the nonmonotonic relationship of density with temperature for water near T_c is reported in *SI Appendix*, section C and Fig. S3). During cold weather conditions when the lake is close to freezing, colder water (less than T_c) floats to the top and warmer water (more than T_c) sinks. Consequently, the coldest water, which sits on top of the lake, releases heat under cold weather conditions and freezes to form a layer of ice. That is why ice first forms on top of water bodies. The tem-

perature structure in shallow ice-covered lakes is characterized by a continuous increase from $0\ ^\circ$C at the ice–water interface up to T_c or higher at the bottom layers in the deep parts of the lake (5). A research report on the ice-covered Karelian lakes found that at the ice formation, a weak stable stratification existed in the lakes with average temperatures about $1\ ^\circ$C. When there is a strong stratification, the turbulent mixing tends to be suppressed. While the temperature exceeds T_c convection develops and it is important for the flow dynamics in the water beneath the ice (6). This water density anomaly results in a complex coupling between the ice layer, the gravitationally stably stratified layer of fluid ($0 < T \le T_c$), and the unstably stratified layer ($T > T_c$, with convective instability) (7–15). The stably stratified layer always exists in the ice–water system, but its strength may be enhanced or depleted under different levels of turbulence.

Connecting to the complex fluid dynamics in the water, the evolution of the ice front and the phase change at the interface show very rich dynamics, which recently have received increasing attention. Rayleigh–Bénard (RB) convection, a fluid layer confined between a cold top plate and a hot bottom plate (16–20), is an ideal model system to study the aforementioned coupled

---

Significance

Landscapes, resulting from ice–water interactions coupled with solidification/melting, are ubiquitous in nature, yet most previous studies have not considered the rich fluid dynamics induced by water density anomaly underneath the moving ice front, which can drastically change system behaviors. By experiments, numerical simulations, and theoretical modeling, we investigate water solidification and its dynamical coupling with (turbulent) convective flows. We reveal four distinct regimes and develop a theoretical model capable of accurately capturing ice thickness and icing timescales. Physical mechanisms revealed from this study, when applied to geological recordings of lake ice, can provide an indicator of climate change. The current investigations offer deeper insight into understanding the coupling between phase change and stratification in marine, geophysical, and astrophysical systems.

ENGINEERING

dynamics. Various studies have been performed on the flow in the RB system with freezing or melting boundary conditions. The focus has been on the behaviors of global quantities such as the heat flux, the kinetic energy, and the dynamics of the ice–water interface morphology with a melting phase-change boundary in the RB system (21–24); pattern selection and instability analysis with a moving solid–water interface (25, 26); the bistability of the equilibria induced by different initial conditions (27, 28); melting in double diffusive convection (29–31); and the influences of different container shapes on the melting and convection of phase change materials (32–34).

While most of these studies consider the interaction of phase change with the convective motions in the fluid, yet several crucial ingredients have not been fully taken into consideration, notably the water density anomaly and the real physical properties of the ice and water. These ingredients are crucial to realistically capturing the growth of the ice layer and the dynamical coupling mentioned above. For example, in geophysical flows, with a typical water temperature in winter of the range $0 \sim 15$ °C (see examples of historical Lake Erie temperatures from the National Weather Service) (35), it is essential to consider the realistic natural configurations to make correct predictions, e.g., how thick the ice can form and how long it takes to arrive at the equilibrium state for a given environmental condition. What's more, correctly predicting the ice formation timescale can provide a reliable indicator of climate change (36–39).

In this work, we combine experiments, numerical simulations, and theoretical modeling to study the coupled dynamics of freshwater solidification and the surrounding fluid dynamics, properly accounting for the water density anomaly and the real physical properties of ice and water. We aim to reveal how the growth of freshwater ice depends on the environmental conditions.

Results and Discussion

Experiments and Simulations. The experiments are performed in a Rayleigh–Bénard convection system of cuboid shape (aspect ratio $\Gamma = L_x/H = 1$, and $L_y = H/4$, where L_x, L_y, and H are the system length, width, and height) heated up from the bottom and cooled down from the top. Water, as the working fluid, is deionized, ultrapured and degassed. The top plate temperature, T_t, and bottom plate temperature, T_b, are imposed by a water-circulating bath, with $T_t < T_\phi$ and $T_b > T_\phi$ (T_ϕ is the water freezing point, $T_\phi = 0$ °C). In such a configuration, ice starts forming from the top plate and it grows until its saturation thickness. During the experimental process, there is a volume change induced by thermal expansion of water and water–ice phase change, so an open expansion vessel is connected to the experimental cell, allowing one to quantify the volume change, and therefore the pressure in the system remains the atmospheric pressure. By monitoring the water volume change inside the expansion vessel, the evolution of the spatial average ice thickness can also be calculated (details are shown in *SI Appendix, sections A and B and Figs. S1 and S2*). In addition to the experiments, the numerical simulations are carried out using lattice-Boltzmann method (LBM) numerical code (22, 40, 41). In the simulations, we consider the density anomaly, the source term from the latent heat at the ice front (42), and the correction for the governing equations when the investigated domain consists of heterogeneous media, i.e., ice and water phases with different thermal conductivities (*SI Appendix, section E*) (43). Two-dimensional ($\Gamma = L_x/H = 1$) and three-dimensional simulations are conducted ($\Gamma = L_x/H = 1$, $L_y = H/4$, same as the experimental cell, with L_y being the system width), and the boundary conditions are no-slip for the velocity, adiabatic at the sidewalls, and constant temperatures at the top and bottom plates. The initial condition is still fluid at uniform temperature, T_b. We assume

thermophysical properties to be constant except for the density in the buoyancy term. The real water density property near T_c is well described with the equation $\rho = \rho_0(1 - \alpha^*|T - T_c|^q)$, where α^* is not the usual thermal expansion coefficient but has units of K^{-q} with $q = 1.895$ and $\alpha^* = 9.30 \times 10^{-6}(K^{-q})$. This equation gives the maximum density of water $\rho_0 = 999.972$ kg/m^3 at $T = T_c$ (44) (*SI Appendix, section C and Fig. S3*).

One important control parameter of the system is the Rayleigh number, Ra_e, which is the dimensionless thermal forcing, and its definition formula is explained below (more details are shown in *SI Appendix, section D*). Another important control parameter is the Stefan number which relates the sensible heat to the latent heat, $Ste = L/C_{pi}(T_\phi - T_t)$, with C_{pi} being the isobaric heat capacity of ice and L the latent heat of solidification. To make sure that the fluid dynamics of the water region are the only influencing factor for the ice evolution, the top temperature, T_t (correspondingly also the Stefan number), both in experiments and simulations is fixed at a typical value for winter, which we select as $T_t = -10$ °C and thus the Stefan number $Ste \approx 20$. The bottom plate temperature, T_b (connected to Rayleigh number to be explained below), is varied in a wide parameter regime, i.e., in experiments 3.8 °C $\leq T_b \leq 8$ °C and in simulations 0.5 °C $\leq T_b \leq 15$ °C (typical water temperature in winter). We employ laboratory experiments to ensure that the simulations capture all relevant aspects of the physics. The results from the experiments act as the validation for the results from the simulations. On the other hand, simulations can provide more detailed information about the investigated system, and also it is easier to change the values of the control parameters in numerical simulations rather than those of the experiments in the laboratory. So we conduct numerical simulations in a wider and more systematic parameter range than that of the experiments.

An important response to the imposed Ra_e and Ste is the overall heat flux transported vertically from bottom to top. The dimensionless heat flux is Nusselt number, Nu (more details are shown in *SI Appendix, section D*).

The Final Average Ice Position. We first compare the final average ice position, h_0, which depends on the bottom plate temperature from the experiments, the two-dimensional (2D) and three-dimensional (3D) simulations, and from the theoretical model (the details of the model are discussed later; recall that we use a fixed top temperature ($T_t = -10$ °C) as a typical example; nevertheless, it should be noted that in real natural situations, h_0 may also be influenced by other factors) (*Results and Discussion*).

Fig. 1*A* is a photograph of the experimental domain at $T_b \approx 8$ °C when the system has reached the statistical equilibrium state. With the same operating conditions, the visualization from the 3D simulation of the ice position and the temperature field in the fluid phase at the statistical equilibrium state is shown in Fig. 1*B*. As shown in Fig. 1 *A* and *B*, the ice–water interface and its position is similar in the experiment and the numerical simulation in the same condition. Varying bottom plate temperature, T_b, in a large temperature range, the spatially averaged ice position at the equilibrium state as a function of T_b is shown in Fig. 1*C*. Depending on T_b, the system may end up in a diffusive state (refer to the green shaded area in Fig. 1*C*) or in a convective state. There is good agreement on the height of the spatially averaged ice–water interface among the experiments and the 2D and 3D simulations as well as the theoretical model with considering the water density anomaly (see Fig. 1*C*, in which E, S, and M stand for experiment, simulation, and model, respectively). However, it is noteworthy that when neglecting the water density anomaly, the prediction of ice position from the model (violet line and green dashed line in Fig. 1*C*) deviates dramatically from the real value. The violet line is under the assumption that the thermal expansion coefficient, α, is a fixed value, which is evaluated at the mean temperature of the
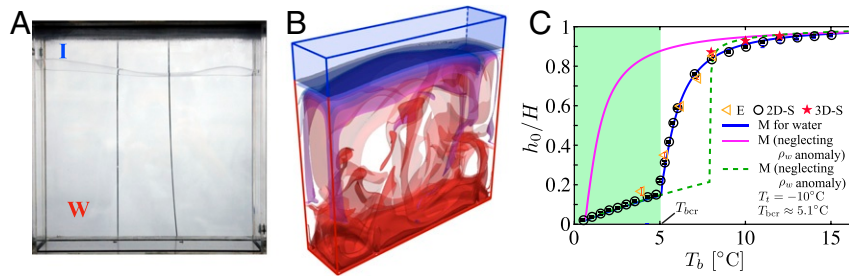
Fig. 1. (*A*) Picture of the experimental domain. The system is heated up at the bottom (above the water freezing point $T_\phi = 0\ °C$) and cooled down from the top (below T_ϕ). To focus on how the fluid dynamics of the water region influence the process of ice formation, the top temperature, T_t, is fixed both in experiments and simulations at a typical value in the winter (which is chosen to be $T_t = -10\ °C$). The case shown in *A* is at the statistical equilibrium state with $T_b \approx 8\ °C$ (to give an impression of the approximate timescale of reaching an equilibrium state, it takes a few hours to a few days in the highly convective state and purely conductive state ($T_b < T_c$)), where "I" stands for ice and "W" for water. (*B*) Visualization of the temperature field across the numerical domain at the statistical equilibrium state (3D simulation for $T_b = 8\ °C$ and $T_t = -10\ °C$). The blue-colored domain is in the ice region. The ice–water interface is drawn in dark blue. (*C*) The comparison of spatial-average ice–water interface from the experiments (triangles) and the 2D (circles) and 3D (stars) simulations, as well as the theoretical model (in the key, E, 2D-S, 3D-S, M for water, and M (neglecting ρ_w anomaly) stand for experiments, 2D simulation, 3D simulation, model for water, and model for water without considering the water density anomaly, respectively; blue line, with considering water density anomaly at T_c; violet line, without considering water density anomaly at T_c), and the thermal expansion coefficient α is evaluated at the mean temperature of the investigated range of T_b ($\sim 7\ °C$); green dashed line, without considering water density anomaly at T_c, and the thermal expansion coefficient α is a function of temperature, which is evaluated at the mean temperature T_{mean} of the water region for each bottom plate temperature T_b, which is $T_{mean} = (T_b + T_\phi)/2$. The green-shaded area shows the temperature range corresponding to the diffusive regime of the system. T_{bcr} is the critical bottom plate temperature ($T_{bcr} \approx 5.1\ °C$, depending on the model results) above which the system ends up in a convective state. The error bars for the experiments (inside the triangles and comparable to the symbol size) come from the measurement errors (more details are reported in *SI Appendix*, section B). The error bars for the simulations (inside the circles) are smaller than the symbol size represent the maximum level of difference between the 2D and 3D simulations.

investigated range of T_b ($\sim 7\ °C$). One may argue that α itself can change with the temperature; then we show the green dashed line, and here α is evaluated at the mean temperature T_{mean} of the water region for each bottom plate temperature T_b, which is $T_{mean} = (T_b + T_\phi)/2$. Nevertheless, the trend from the model without considering the water density anomaly (the violet line and green dashed line in Fig. 1*C*) is very different from the real situation (the blue line in Fig. 1*C*). The key reason is that the stably stratified layer (with temperature ranging from T_ϕ to T_c), which results from the density anomaly of water, is crucial for the dynamics of the system. The results from the experiments and 2D and 3D simulations agree well with each other, which indicates the simulations are reliable, and therefore in the following we explore the complex nature of the coupled dynamics mostly via 2D simulations as these allow us to more efficiently scrutinize the phenomena in a wide range of parameters.

The Coupled Dynamics of the Ice Growth with the Fluid Motion. To investigate the physical mechanism, we highlight four distinct regimes based on the phenomenology of the equilibrium state as the bottom plate temperature increases from below to above T_c (Fig. 2 *A–D*). The four regimes that will be considered are as follows, where the first two letters of the acronyms specify the feature of stratification, which can be either stably stratified (SS) or unstably stratified (US), and the third letter of the acronyms specifies the mode of heat transport (and fluid motion) which can be either diffusion (D) or convection (C): 1) regime 1, SSD with flat ice ($T_b \leq T_c$); 2) regime 2, SSD + USD with flat ice ($T_c < T_b \leq 5.1\ °C$); 3) regime 3, SSD + USC with flat ice ($5.1\ °C < T_b \leq 6.9\ °C$); and 4) regime 4, SSD + USC with deformed ice front ($T_b > 6.9\ °C$).

The boundaries between different regimes depend on the bottom plate temperature (here, around the threshold between each regime, we did simulations with 0.1-K increments to better identify the transition values). Fig. 2 *A–D* shows typical cases from all four regimes from the simulations. Next, we discuss the details of the four regimes.
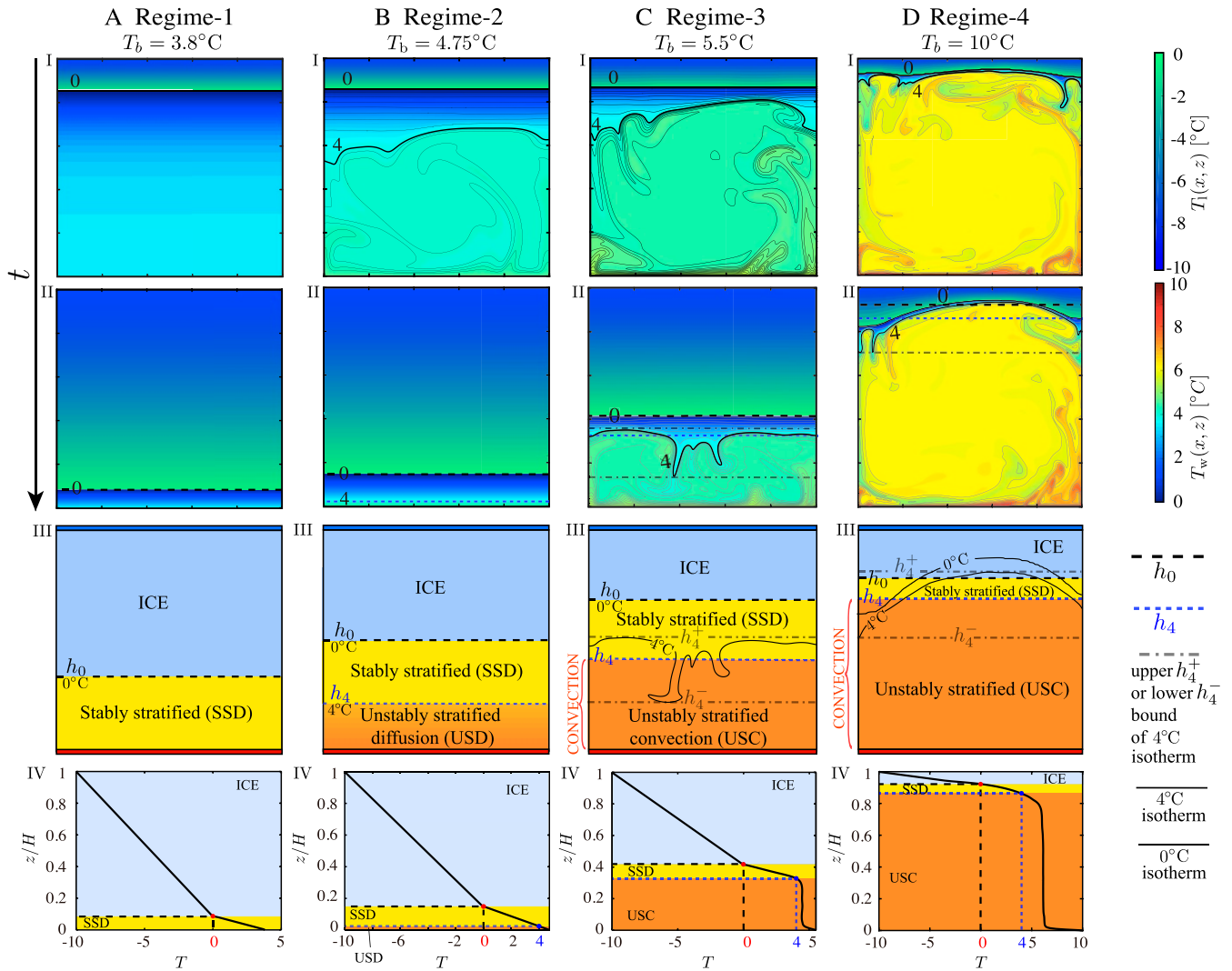
Regime-1 ($T_b \leq T_c$). Fig. 2*A* shows a typical case in this regime. The system is in a stably stratified state with purely diffusive heat transfer all of the way from the beginning (Fig. 2 *A, I*) until the

end (Fig. 2 *A, II*); the corresponding sketch, which shows different layers at the statistical equilibrium state in the system, can be seen in Fig. 2 *A, III*. The ice–water interface is always flat, indicating that the instantaneous 0 °C isotherm overlaps with the average position of the ice front, h_0. The temperature profiles are linearly dependent on the height in both the ice and water phases, with the different slopes corresponding to the different thermal conductivity in ice and water (Fig. 2 *A, IV*).

Regime-2 ($T_c < T_b \leq 5.1\ °C$). Raising the bottom plate temperature into this regime, the gravitationally unstably stratified layer (from the level of the bottom plate to the spatially averaged level of T_c denoted as h_4, namely the horizontally average temperature is T_c at $z = h_4$, with the temperature ranging from T_c to T_b) emerges beneath the gravitationally stably stratified layer (from the level of h_4 to h_0 with the temperature ranging from T_ϕ to T_c; yellow shaded area in Fig. 2 *B, III*). When $T_b > T_c$, to know beforehand whether the heat transfer regime is diffusive or convective during the transient state and the statistical equilibrium state, we define the effective Rayleigh number, Ra_e, based on the thickness of the water region from the bottom plate to the spatially average level of T_c and the corresponding temperature difference, which reads (28)

$$\mathrm{Ra}_e = \frac{(\Delta\rho/\rho_0)g(h_4)^3}{\nu\kappa} = \frac{g\alpha^*(T_b - T_c)^q(h_4)^3}{\nu\kappa}, \qquad [1]$$

with g being the gravitational acceleration, ν the kinematic viscosity, and κ the thermal diffusivity. Due to the initial conditions, the system starts from convection in the gravitationally unstably stratified layer, with the T_c isotherm deformed (Fig. 2 *B, I*), where $\mathrm{Ra}_e \sim 10^8 \gg \mathrm{Ra}_{cr} \approx 1{,}708$ (Ra_{cr} is estimated by the linear instability analysis, which has been intensively validated in the references) (45–47). As the ice grows, the effective height, h_4, shrinks and Ra_e consequently decreases. And thus the system ends up at a diffusive state in the entire water layer (SSD + USD) with effective Rayleigh number in US layer $\mathrm{Ra}_e \sim 10$ smaller than Ra_{cr}. This also explains why the T_c isotherm becomes flat in the end (Fig. 2 *B, II*), and the corresponding sketch is shown in Fig. 2 *B, III*. The entire system is in a

Wang et al.
How the growth of ice depends on the fluid dynamics underneath

PNAS | 3 of 8
https://doi.org/10.1073/pnas.2012870118

Fig. 2. The phenomenology of temporal dynamics and the feature at the statistical equilibrium states in the four regimes. Typical case visualizations from regimes 1 to 4: (*A*) $T_b = 3.8\ °C$, (*B*) $T_b = 4.75\ °C$ (Movie S1), (*C*) $T_b = 5.5\ °C$ (Movie S2), and (*D*) $T_b = 10\ °C$ (Movie S3). Shown are different time instances of temperature field for four typical regimes of the simulations (*A–D, I* and *II*). The sketches in *A–D, III* depict the coupled different layers of the system at the statistical equilibrium state in regimes 1 to 4, respectively, in which the interfaces (horizontal lines) between neighboring layers (different color shaded areas) are space-averaged values. The dashed black line is for h_0 (the final average ice position); dotted blue line is for h_4 (the final average T_c isotherm); thick black curved lines are for instantaneous $0\ °C$ and T_c isotherms, respectively; and dashed-dotted lines are for the upper bound h_4^+ and lower bound h_4^- of instantaneous T_c isotherms. In *A–D, IV* the temporal and space-averaged temperature profiles at the statistical equilibrium state corresponding to the four typical cases are shown. In *A–D, III* and *IV* the blue-shaded, yellow-shaded, and orange-shaded areas denote ice (ICE), stably stratified layer (SS), and unstably stratified layer (US), respectively. To make the flow structures more visible, two approaches are applied: 1) Two color bars for the temperature field corresponding to ice region ($T_I(x, z)$) and water region ($T_w(x, z)$) are shown on the right of *D, I* and *II*; 2) *A, I, C, I* and *II*, and *D, I* and *II* show more isotherms (thin black lines) except for $0\ °C$ and T_c isotherms (thick black lines), which are designed to make the hot and cold plumes more noticeable.

diffusive state with a linear temperature profile (Fig. 2 *B, IV*) similar to that in regime 1.

Regime 3 (5.1 °C < T_b ≤ 6.9 °C). As T_b is in regime 3, with temperature ranging from 5.1 °C to 6.9 °C, there are rich fluid dynamics in the fluid layer below the ice. The system ends up in the convective state with $\mathrm{Ra_e} \sim 10^5$ (Fig. 2 *C, II*). We can see hot plumes form at the bottom plate. During the lifetime of hot plumes, they detach from the bottom plate shortly after being generated; the plumes accumulate and become coherent plumes, which rise through the bulk region while experiencing heat exchange with the fluid around; if in a classical Rayleigh–Bénard system, they would later on go through the cold boundary layer below the flat T_c isotherm where they give out most of the energy and slow down to stop; however, in the stably and unstably stratified coupled system presented here, bunches of plumes

can impact on and deform the T_c isotherm because of turbulent bursts. The T_c isotherm is no longer flat but develops some spatial variations (thick black line in Fig. 2 *C, II*). The region from the spatially average height, h_4, of the instantaneous T_c isotherm to its upper bound, h_4^+, belongs to the gravitationally stably stratified layer but there are also some warmer patches of fluid with the temperature larger than T_c from the unstably stratified layer. Due to mass conservation, the same amount of fluid, with a temperature smaller than T_c coming from the gravitationally unstably stratified layer, goes downward below the level of h_4 (see the downward cold plumes in the region from the lower bound of the instantaneous T_c isotherm h_4^- to h_4 in Fig. 2 *C, III*; the flow is convection dominated in that the estimated Peclet number in the current regime is of order $10^2 \sim 10^3 \gg 1$; the Peclet number denotes the relative importance of

convection with respect to diffusion and is defined as $Pe = LU/\kappa$ (48), where U is the characteristic velocity which is taken as the free-fall velocity scale with corrections $U = 0.2\frac{\nu\sqrt{RaPr}}{h_4}$ for buoyancy driven convection (49), and L is the characteristic length scale of the flow which is based on the unstably stratified layer, i.e., L is the thickness of the unstably stratified layer, $L = h_4$). In other words, due to the nonmonotonical behavior of water with respect to the temperature, on average there is a stably stratified layer with diffusive heat transfer (SSD, from the level of h_4 to that of h_0) and unstably stratified layer with convective heat transport (USC, from the level of the bottom plate to that of h_4); however, instantaneously because of the penetration, there is a strong fluid exchange between SSD and USC as indicated by the deformation of the instantaneous T_c isotherm. Because of the shield of SSD where there is still a horizontal layer with fluid temperature purely smaller than T_c (from h_4^+ to h_0), the ice–water interface is still flat in regime 3. In this regime, the temperature profile in the entire water layer is not linear (Fig. 2 C, IV). In the entrainment layer (from the level of h_4^- to the level of h_4^+) and underneath USC, the temperature profile reflects the turbulence-induced mixing: There is a hot thermal boundary layer attached to the bottom plate, a well-mixed bulk region of nearly uniform temperature, and a cold thermal boundary layer.

Regime 4 ($T_b > 6.9$ °C). Upon further increasing T_b to above 6.9 °C, the level of the upper bound of the instantaneous T_c isotherm, h_4^+, is even higher than the spatially averaged level of ice position h_0, which indicates strong thinning of the thermal boundary layer by the plumes. On the plume-impact region, ice melts and forms a concave interface due to extra heat input. We can see that there is no horizontally stably stratified layer with fluid temperature purely smaller than T_c which can shield the ice front from the turbulent convective motion. The T_c-isotherm line is not in a well-defined position; instead, it displays intensive spatial fluctuations due to strong turbulent plumes, resulting in local melting or freezing of the ice front. The water layer consists of a very wide range of USC at the equilibrium state (Fig. 2 D, II). The temperature profile is similar to that in regime 3 but with a much thicker water layer thickness and a much thinner ice layer. The asymmetrical feature of the thermal boundary layers in the water does not occur in the classical Rayleigh–Bénard convection, but it has also been found in ref. 15, in which they investigated the penetrative convection based on the Prandtl number $Pr = 1$ which is different from the value we used ($\sim$10). In their work, the reported asymmetrical feature of the thermal boundary layers (figures 9–11 in ref. 15) is similar to that found in regime 3 (Fig. 2 C, IV) and regime 4 (Fig. 2 D, IV) of the current study, when the system has the coexistence of the stably and unstably stratified layers.

In summary, we can see that the heat transfer regimes of diffusion and convection can be even switched dynamically during the evolving process due to the fact that the USC thickness is changing, so the system may end up in a diffusive or convective state depending on the final effective Rayleigh number Ra_e (which varies with T_b). The statistical equilibrium state depends on the bottom plate temperature, T_b. Next, we assess the detailed ice dynamics in a more quantitative perspective.

The flow is highly dynamic in regimes 3 and 4, and the intricate nature of the intensive interaction among the ice front, the entrainment layer, and the unstably stratified layer leads to high fluctuations of T_c and T_ϕ isotherm varying in a range (gray-shaded area and red-shaded area in Fig. 3). Nevertheless, the global responses of the system, i.e., the horizontal-spatial-average thicknesses of the ice–water interface, h_0 (where the horizontally average temperature is 0 °C), and h_4 (where the horizontally average temperature is T_c), match up well to the one-dimensional model for water (discussed below) except
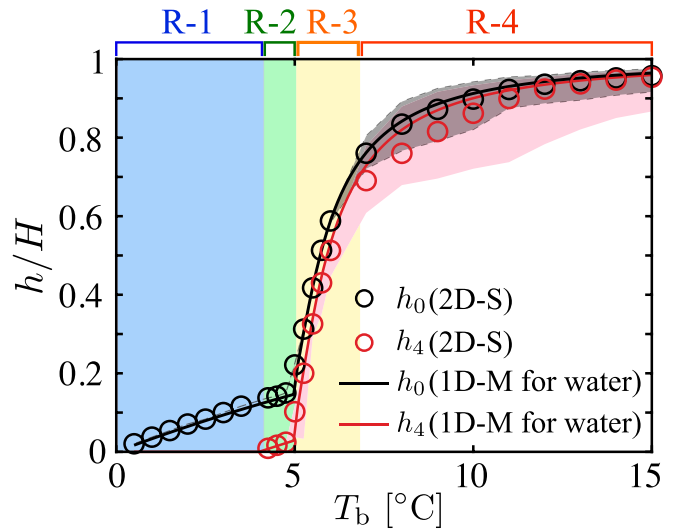
Fig. 3. The complex phenomenology emerging from the tight interplay among ice front, stably stratified layer, and unstably stratified layer: comparison of the theoretical model (black thick line for h_0, red thick line for h_4) and the simulations featuring the real nature of fluctuations, with circles being the average values (black circles for h_0, red circles for h_4), and gray-shaded area and red-shaded area indicating the spatial fluctuation of instantaneous ice–water interface and T_c isotherm. The blue-shaded area indicates regime 1 (R-1), the green-shaded area regime 2 (R-2), the yellow-shaded area regime 3 (R-3), and the remaining area regime 4 (R-4). In regime 4 where T_b (i.e., Ra_e) is high, the predictions for h_4 deviate a bit from the theoretical model due to the intensive interaction among different layers.

for some deviations in regimes 3 and 4. The ice–water interface and the T_c isotherm attach to and adjust to each other, which results in a self-organizing large-scale circulation, and the overall effects shape the ice front as shown in Fig. 2 D, II.

Theoretical Model. The ice thickness can be properly predicted by taking into account the water density anomaly and the known scaling properties of turbulent thermal convection (namely the Nusselt number–Rayleigh number relation) (18). Next, we introduce the theoretical model and we consider two situations: 1) for statistical equilibrium states and 2) for the time-dependent transient states. Here, we assume one-dimensional geometry and all of the notations are consistent with those in Fig. 2 A–D, III (more details about the theoretical model are reported in *SI Appendix, section D*).

1) Theoretical model for water: statistical equilibrium state. When the system has reached the statistical equilibrium state, there is an energy balance between the heat flux through the ice layer and that through the water layer. When $T_b > T_c$, the water layer consists of a stably stratified layer (from T_ϕ to T_c) and an unstably stratified layer (from T_c to T_b). Based on the heat flux balance, the average thicknesses of the ice layer ($H - h_0$), stably stratified layer ($h_0 - h_4$), and unstably stratified layer (h_4, exists when $T_b > T_c$) at the equilibrium states can be evaluated.

In the temperature range $T_b \leq T_c$. The system is in a diffusive state and independent of the water layer thickness, the total water layer is stably stratified. According to the conservation of heat flux, we can obtain

$$k_I \frac{T_\phi - T_t}{H - h_0} = k_w \frac{T_b - T_\phi}{h_0}, \qquad [2]$$

where k_I and k_w are the thermal conductivity of ice and water, respectively. Recall that $T_\phi = 0$ °C, from which we obtain the results on the thicknesses as follows:

Wang et al.
How the growth of ice depends on the fluid dynamics underneath

PNAS | 5 of 8
https://doi.org/10.1073/pnas.2012870118

$$\begin{cases} H - h_0 = \dfrac{-k_I T_t}{k_w T_b - k_I T_t} H, \\ h_0 = \dfrac{k_w T_b}{k_w T_b - k_I T_t} H. \end{cases} \quad [3]$$

In the temperature range $T_b > T_c$. We assume that the interfaces of the ice front and that between the stably stratified and the unstably stratified layers are both flat, based on the heat flux balance between the gravitationally unstably stratified layer (from the level of the bottom plate to the spatially average level of T_c denoted as h_4, namely the horizontally average temperature is T_c at $z = h_4$, with the temperature ranging from T_c to T_b) and the gravitationally stably stratified layer (from the level of h_4 to h_0, with the temperature ranging from T_ϕ to T_c),

$$\begin{cases} k_I \dfrac{T_\phi - T_t}{H - h_0} = k_w \dfrac{T_c - T_\phi}{h_0 - h_4}, \\ k_I \dfrac{T_\phi - T_t}{H - h_0} = Nu\, k_w \dfrac{T_b - T_c}{h_4}. \end{cases} \quad [4]$$

The model for the heat flux in the unstably stratified layer is in the form of Nusselt number as a function of Rayleigh number (Nusselt number is the dimensionless heat flux defined as $Nu = \frac{\partial_z T|_{z=0}}{(T_c - T_b)/h_4}$). The Rayleigh number dependence of Nu can be obtained from the simulations and is consistent with that of the classical Rayleigh–Bénard in the same parameter regime (18, 50), suggesting that the model we build is of a general form (more details are reported in *SI Appendix*, section D).

By this statistical equilibrium-state model, the final ice position, as a function of T_b (Figs. 1C and 3), and the T_c isotherm position, as a function of T_b, can be calculated, which show a good agreement with the results from experiments as well as simulations.

2) Theoretical model for water: transient state. Following the analytical methods for the classical Stefan problem (51), since the time-dependent evolving interface between ice and water (denoted as $z = h_0(t)$, where $h_0(t)$ is the height at which $T_w(h_0(t), t) = T_\phi$) is a priori unknown, a part of the solution will be to determine the boundary. As the phase transition occurs, there will be volume change due to the density difference between water and ice as well as the thermal expansion effect. To simplify the problem, here we ignore this volume variation. Further, we consider the one-dimensional heat transfer problem and assume that the physical properties are invariant with temperature while their values are different for the ice and water phase; the ice–water interface is fixed at phase change temperature T_ϕ (recall $T_\phi = 0\,^\circ C$).

When $T_b \leq T_c$, the basic control equations are

$$\frac{\partial T_I(z, t)}{\partial t} = \alpha_I \frac{\partial^2 T_I(z, t)}{\partial z^2}, \ 0 < z < h_0(t), \quad [5]$$

$$\frac{\partial T_w(z, t)}{\partial t} = \alpha_w \frac{\partial^2 T_w(z, t)}{\partial z^2}, \ h_0(t) < z < H, \quad [6]$$

where α is the thermal diffusivity, and the subscripts "I" and "w" denote ice and water phase, respectively. The boundary conditions read

$$\begin{gathered} T_w(0, t) = T_b, \\ \lim_{z \to h_0(t)^-} T_w(z, t) = \lim_{z \to h_0(t)^+} T_I(z, t) = T_\phi, \\ T_I(H, t) = T_t, \end{gathered} \quad [7]$$

where the superscripts "+" and "−" indicate the direction when taking the limit, namely from smaller than $h_0(t)$ toward $h_0(t)$

and from larger than $h_0(t)$ toward $h_0(t)$, respectively. The energy balance at the ice–water interface is

$$L\rho_I \frac{dh_0(t)}{dt} = k_I \frac{\partial T_I(z, t)}{\partial z}\Big|_{z=h_0(t)^+} - k_w \frac{\partial T_w(z, t)}{\partial z}\Big|_{z=h_0(t)^-}. \quad [8]$$

From Eqs. **5–8**, we obtain the solutions for temperature distributions in the ice and water,

$$\begin{gathered} T_w(z, t) = T_b - \frac{T_b}{erfc(\lambda_w)} erfc\left(\frac{Z}{2\sqrt{\alpha_w t}}\right), \\ T_I(z, t) = T_t - \frac{T_t}{erf(\lambda_I)} erf\left(\frac{Z}{2\sqrt{\alpha_I t}}\right), \end{gathered} \quad [9]$$

where $Z = H - z$, erf is the error function $(erfc(x)) = 1 - erf(x))$, and

$$\lambda_w = \frac{H - h_0(t)}{2\sqrt{\alpha_w t}}, \ \lambda_I = \frac{H - h_0(t)}{2\sqrt{\alpha_I t}}. \quad [10]$$

When $T_b > T_c$, the effective Rayleigh number can be calculated and the interface energy balance takes the form

$$L\rho_I \frac{dh_0(t)}{dt} = k_I \frac{\partial T_I(h_0(t)^+, t)}{\partial z} + Nu\ k_w \frac{T_b - T_\phi}{h_0(t)}. \quad [11]$$

Based on Eqs. **5** and **11** with boundary conditions Eq. **7**, the position of the ice–water interface as a function of time can be solved, and therefore we can predict the temporal evolution of the global icing process (Fig. 4B) (more details are reported in *SI Appendix, section D*).

Growth Dynamics of the Ice Layer. The coupled interactions between the stably and the unstably stratified layers play a major role in determining the final saturation thickness of the ice layer and the time it takes to reach the saturation state (here we define the saturation time, t^*, as the time when the ice thickness reaches 90% of the final statistical equilibrium state thickness). At early stages of the evolution, the conductive heat transfer within the ice layer dominates versus the convective heat transfer within the liquid; because the ice layer is thin where the temperature gradient is large, correspondingly, the conductive heat flux is large. This conduction-dominated early evolution stage yields leading-order behavior of the ice thickness with $(H - h_0)/H \propto t^{0.5}$ at early times even with convective heat fluxes in the liquid (Fig. 4A). The ice growth deviates from the early leading-order behavior due to the convective flows in the water layer. The saturation time t^* versus the bottom plate temperature is shown in Fig. 4B, which clearly shows a good agreement between simulations (black symbols) and experiments (orange symbols). We also compare the experimental and numerical results with those in the theoretical model. They show a good agreement except that there is some deviation in regimes 2 and 3, which may be due to the complex dynamics around the onset of convection. Further, the coexistence of stably and unstably stratified layers leads to the effective convective region (corresponding to the unstably stratified layer) being smaller than the entire water depth, which may contribute to the discrepancy. Based on the investigated parameter regime, it is revealed that the temperature of the bottom surface has major effects on the icing time. To give the reader an impression of the physical saturation timescale, for example, when the bottom plate increases from $T_b = 0.5\,^\circ C$ to $T_b = 15\,^\circ C$, the saturation time can vary from a few days to a few hours.

Here, we use a fixed top temperature ($T_t = -10\,^\circ C$) as a typical example; nevertheless, it should be noted that in real natural situations, the icing dynamics may also be influenced by the cooling conditions, whole water layer depth, and other factors, to
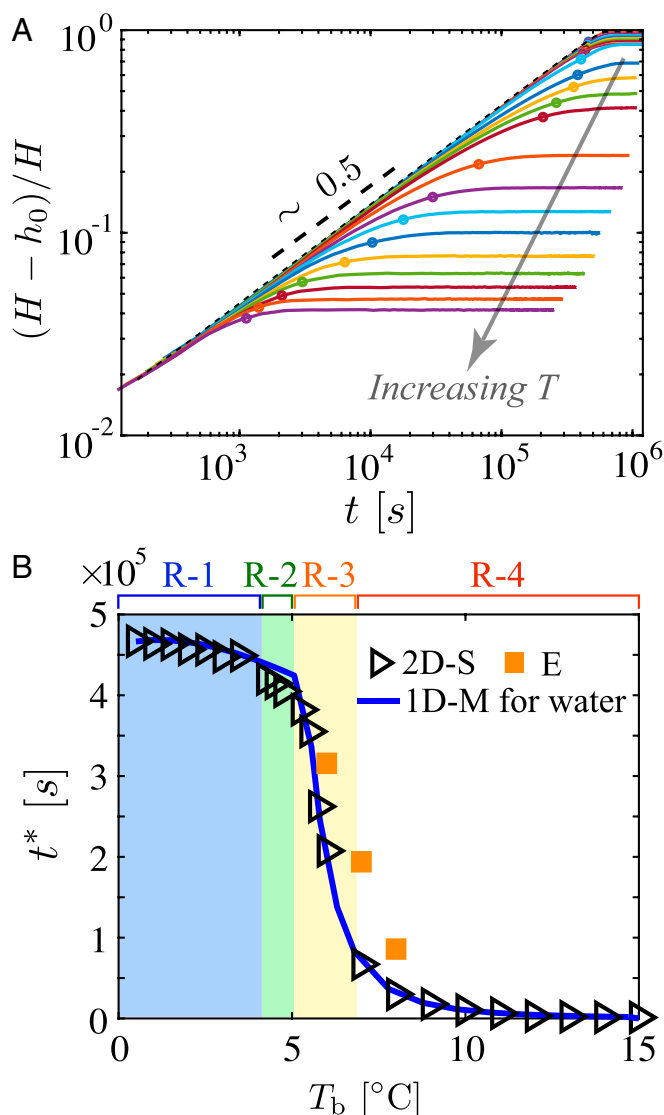
Fig. 4. Dynamics of the ice growth. (*A*) Time evolution of the average ice thickness for various T_b. The parameters are $T_t = -10$ °C and 0.5 °C $\leq T_b \leq$ 15 °C. The gray arrow indicates the direction of increasing T_b. The circles show the saturation time (when ice thickness is increasing to a value of 90% of that in the statistical equilibrium state). (*B*) The saturation time as a function of T_b. The blue-shaded area specifies regime 1 (R-1), the green-shaded area regime 2 (R-2), the yellow-shaded area regime 3 (R-3), and the remaining area regime 4 (R-4).

which our findings are still applicable and the model is easy to extend to general situations.

Conclusions and Outlook

By combining experiments, simulations, and theoretical modeling, we systematically investigated the coupled dynamics between flow and ice growth for different levels of stratification instability (i.e., higher T_b signifies increasingly unstably stratified). We revealed that the dynamics of the ice thickness can be accurately predicted only by properly taking into account the water density anomaly, in combination with the known Grossmann–Lohse theory (18) scaling properties of turbulent thermal convection. We uncovered the rich coupling dynamics among the ice–water interface and the stably and unstably stratified layers.

Four regimes were identified depending on T_b (regimes 1 to 4), which show the different degrees of interactions with respect

to the activities in the water layer. It is noteworthy that turbulent bursts from the convective unstably stratified layer can penetrate above the T_c and induce the entrainment layer in regime 3. However, as long as the ice still enjoys the protection of the horizontally continuous stably stratified layer (where the heat transfers diffusively, SSD), the system terminates with a flat ice–water interface, regardless of the water layer ending up in a convection (regime 3) or a conduction state (regimes 1 and 2). Higher thermal intensity (namely high T_b) leads to the deformation of the ice (Fig. 2 *D*, *II*), which indicates that some spots of the ice block could become thin and vulnerable, and in the case of river or lake ice, these spots may act as an initial breakout point. This information is of great importance in deicing and dredging waterways to provide a more convenient, effective, and smooth freight transportation system in winter. Further, we showed that, up to a moderate level of turbulence (regimes 1 to 3), the spatially and temporally averaged ice thickness at the equilibrium state can be well predicted by the theoretical model, suggesting robust predictability of the model with the consideration of the density anomaly.

We found that the ice grows diffusively until the system slowly arrives at the energy balance state and the saturation time can be also well predicted by the theoretical model. Within the investigated parameter regime, the equilibrium time for the ice growth decreases from a few days to a few hours upon increasing T_b, suggesting different environments can tune the final state and its icing time. It is noteworthy that our findings can be extended to general situations, such as different environment temperatures and different system sizes, among others.

By modifying the thermal condition of the system, the coupling of stably and unstably stratified layers holds promise for regulating local mixing in devices (devoid of moving parts) with respect to contemporary clinical, pharmaceutical, and chemical applications and is of interest for biologically active elements.

The approach followed in this study, which is based on the matching of controlled laboratory-scale experiments with fully resolved direct-numerical simulations, sets a standard for future explorations on convection coupled to phase-change problems. We note that the current work has uncovered only a subset of the rich possibilities of ice–water dynamics in terms of the parameter space. In future investigations, we plan to continue by studying the effects of container aspect ratio, ice–water interface inclination, dissolved salt, and overburden pressure, the topics of which are of great relevance for better modeling of geophysical and climatological large-scale processes.

Materials and Methods

Below, we provide basic information on the experiments, theoretical modeling, and numerical simulations performed in this work. Further details and additional figures are provided in *SI Appendix*.

Experimental Setup. The turbulent convection coupled with solidification of freshwater experiments was performed in a classical convection setup (*SI Appendix*, Fig. S1A). The experimental cell, of rectangular shape, consists of Plexiglas sidewalls with height $H = 240$ mm (length $L_x = 240$ mm and width $L_y = 60$ mm, i.e., aspect ratio $\Gamma = L_x/H = 1.0$). The working fluid is confined in between the copper top plate (cooled by circulating bath; PolyScience PP15R-40) and the copper bottom plate (heated by circulating bath; Poly-Science PP15R-40). In the experiments, ice forms on the top plate and grows in thickness until the system reaches a statistical equilibrium state. During the phase-change process, there is a volume change. To release the pressure due to volume change induced by phase change, an expansion vessel is connected to the experimental cell through a tube. The expansion vessel is open to the atmosphere so that the pressure of the experimental cell is kept constant. To avoid evaporation of the water in the expansion vessel, we use a thin layer of silicone oil (immiscible with water) to seal the water surface. By monitoring the water level inside the expansion vessel, the spatial average ice position, h_0 (i.e., the ice thickness is $H - h_0$), can be

Wang et al.
How the growth of ice depends on the fluid dynamics underneath

PNAS | 7 of 8
https://doi.org/10.1073/pnas.2012870118

calculated for each bottom plate temperature, T_b (*SI Appendix*, section B). Six resistance thermistors (44000 series thermistor element; *SI Appendix*, Fig. S1*C*) are embedded into the top and bottom plates, respectively. To control the temperature of the setup and to avoid the heat exchange between the experimental cell and the environment, there are two kinds of techniques applied: 1) The experimental cell is wrapped in a sandwich structure of insulation foam, aluminum plate, and insulation foam and 2) a proportional-integral-derivative (PID) controller (*SI Appendix*, Fig. S1*B*) is installed to the setup (more details are reported in *SI Appendix*, sections A and B). The working fluid is deionized and ultrapure water. Before the experiments, water is boiled twice to degas. Since water density inverses at temperature T_c, here we use the nonmonotonic relationship of density with temperature for water near T_c and details are reported in *SI Appendix*, section C.

Theoretical Model. The theoretical modeling takes into account the water density anomaly and assumes a one-dimensional system. It provides predictions for the two following conditions: 1) for statistical equilibrium states and 2) for the time-dependent transient states. We also perform theoretical modeling without considering water density anomaly and prove that in this case the ice position cannot be predicted properly. More details about the theoretical model are reported in *SI Appendix*, section D.

Numerical Simulations. We use the LBM which is able to capture the turbulent convective dynamics in the water phase and also describe the phase change process at the ice–water interface by means of an enthalpy approach. *SI Appendix*, section E provides more details about the relevant equations that govern phase change, fluid flow, and heat transfer solved by the LBM algorithm.

Data Availability. All study data are included in the article and/or *SI Appendix*.

1. P. Meakin, B. Jamtveit, Geological pattern formation by growth and dissolution in aqueous systems. *Proc. R. Soc. A* **466**, 659–694 (2010).
2. T. Alboussiere, R. Deguen, M. Melzani, Melting-induced stratification above the earth's inner core due to convective translation. *Nature* **466**, 744–747 (2010).
3. M. Epstein, F. Cheung, Complex freezing-melting interfaces in fluid flow. *Annu. Rev. Fluid Mech.* **15**, 293–319 (1983).
4. M. G. Worster, Convection in mushy layers. *Annu. Rev. Fluid Mech.* **29**, 91–122 (1997).
5. M. A. Bilello, Water temperatures in a shallow lake during ice formation, growth, and decay. *Water Resour. Res.* **4**, 749–760 (1968).
6. J. Malm, Bottom buoyancy layer in an ice-covered lake. *Water Resour. Res.* **34**, 2981–2993 (1998).
7. G. Veronis, Penetrative convection. *Astrophys. J.* **137**, 641 (1963).
8. A. Arid, T. Koussksou, S. Jegadheeswaran, A. Jamil, Y. Zeraouli, Numerical simulation of ice melting near the density inversion point under periodic thermal boundary conditions. *Fluid Dynam. Mater. Process.* **8**, 257–275 (2012).
9. E. Large, C. Andereck, Penetrative Rayleigh-Bénard convection in water near its maximum density point. *Phys. Fluids* **26**, 094101 (2014).
10. M. Corcione, A. Quintino, Penetrative convection of water in cavities cooled from below. *Comput. Fluid* **123**, 1–9 (2015).
11. B. Ayurzana, T. Hosoyamada, "Phase change simulations of water near its density inversion point by lattice Boltzmann method" in *Proceedings of the 23rd IAHR International Symposium on Ice* (International Association for Hydro-Environment Engineering and Research, 2016), pp. 1–8.
12. Q. Wang, Q. Zhou, Z. Wan, D. J. Sun, Penetrative turbulent Rayleigh-Bénard convection in two and three dimensions. *J. Fluid Mech.* **870**, 718–734 (2019).
13. P. Léard, B. Favier, P. Le Gal, M. Le Bars, Coupled convection and internal gravity waves excited in water around its density maximum at 4°C. *Phys. Rev. Fluids* **5**, 024801 (2020).
14. D. Lecoanet et al., Numerical simulations of internal wave generation by convection in water. *Phys. Rev.* **91**, 063016 (2015).
15. S. Toppaladoddi, J. S. Wettlaufer, Penetrative convection at high Rayleigh-Bénard. *Phys. Rev. Fluid.* **3**, 043501 (2018).
16. E. D. Siggia, High Rayleigh number convection. *Annu. Rev. Fluid. Mech.* **26**, 137–168 (1994).
17. E. Bodenschatz, W. Pesch, G. Ahlers, Recent developments in Rayleigh-Bénard convection. *Annu. Rev. Fluid. Mech.* **32**, 709–778 (2000).
18. G. Ahlers, S. Grossmann, D. Lohse, Heat transfer and large scale dynamics in turbulent Rayleigh-Bénard convection. *Rev. Mod. Phys.* **81**, 503 (2009).
19. D. Lohse, K. Q. Xia, Small-scale properties of turbulent Rayleigh-Bénard convection. *Annu. Rev. Fluid. Mech.* **42**, 335–364 (2010).
20. F. Chillà, J. Schumacher, New perspectives in turbulent Rayleigh-Bénard convection. *Eur. Phys. J. E* **35**, 58 (2012).
21. S. Madruga, J. Curbelo, Dynamic of plumes and scaling during the melting of a phase change material heated from below. *Int. J. Heat Mass Tran.* **126**, 206–220 (2018).
22. B. Rabbanipour Esfahani, S. C. Hirata, S. Berti, E. Calzavarini, Basal melting driven by turbulent thermal convection. *Phys. Rev. Fluids* **3**, 053501 (2018).
23. B. Favier, J. Purseed, L. Duchemin, Rayleigh-Bénard convection with a melting boundary. *J. Fluid Mech.* **858**, 437–473 (2019).
24. O. Satbhai, S. Roy, S. Ghosh, S. Chakraborty, R. Lakkaraju, Comparison of the quasi-steady-state heat transport in phase-change and classical Rayleigh-Bénard convection for a wide range of Stefan number and Rayleigh number. *Phys. Fluids* **31**, 096605 (2019).
25. S. H. Davis, U. Müller, C. Dietsche, *Pattern Selection in Single-Component Systems Coupling Bénard Convection and Solidification* (Kernforschungszentrum, 1983).
26. C. Dietsche, U. Müller, Influence of Bénard convection on solid–liquid interfaces. *J. Fluid Mech.* **161**, 249–268 (1985).
27. G. M. Vasil, M. R. E. Proctor, Dynamic bifurcations and pattern formation in melting-boundary convection. *J. Fluid Mech.* **686**, 77–108 (2011).
28. J. Purseed, B. Favier, L. Duchemin, E. W. Hester, Bistability in Rayleigh-Bénard convection with a melting boundary. *Phys. Rev. Fluids* **5**, 023501 (2020).
29. M. Sugawara, T. F. Irvine, The effect of concentration gradient on the melting of a horizontal ice plate from above. *Int. J. Heat Mass Tran.* **43**, 1591–1601 (2000).
30. M. Sugawara et al., Visual observations of flow structure and melting front morphology in horizontal ice plate melting from above into a mixture. *Heat Mass Tran.* **43**, 1009–1018 (2007).
31. S. Mergui, S. Geoffroy, C. Bénard, Ice block melting into a binary solution: Coupling of the interfacial equilibrium and the flow structures. *J. Heat Tran.* **124**, 1147–1157 (2002).
32. N. S. Dhaidan, J. M. Khodadadi, Melting and convection of phase change materials in different shape containers: A review. *Renew. Sustain. Energy Rev.* **43**, 449–477 (2015).
33. Y. Hu, D. Li, S. Shu, X. Niu, Lattice Boltzmann simulation for three-dimensional natural convection with solid-liquid phase change. *Int. J. Heat Mass Tran.* **113**, 1168–1178 (2017).
34. M. Sugawara, Y. Komatsu, H. Beer, Melting and freezing around a horizontal cylinder placed in a square cavity. *Heat Mass Tran.* **45**, 83 (2008).
35. National Weather Service, Historical Lake Erie temperatures (1927-2019). https://www.weather.gov/buf/Hist_LakeTemps. Accessed 30 May 2020.
36. J. J. Magnuson et al., Historical trends in lake and river ice cover in the northern hemisphere. *Science* **289**, 1743–1746 (2000).
37. M. R. Magee, C. H. Wu, D. M. Robertson, R. C. Lathrop, D. P. Hamilton, Trends and abrupt changes in 104 years of ice cover and water temperature in a dimictic lake in response to air temperature, wind speed, and water clarity drivers. *Hydrol. Earth Syst. Sci.* **20**, 1681–1702 (2016).
38. D. L. Preston et al., Climate regulates alpine lake ice cover phenology and aquatic ecosystem structure. *Geophys. Res. Lett.* **43**, 5353–5360 (2016).
39. M. R. Magee, C. H. Wu, Effects of changing climate on ice cover in three morphometrically different lakes. *Hydrol. Process.* **31**, 308–323 (2017).
40. S. Succi, *The Lattice-Boltzmann Equation: for Fluid Dynamics and Beyond* (Oxford University Press, 2001).
41. C. Huber, A. Parmigiani, B Chopard, M Manga, O Bachmann, Lattice-Boltzmann model for melting with natural convection. *Int. J. Heat Fluid Flow* **29**, 1469–1480 (2008).
42. M. Faden, A. König-Haagen, D. Brüggemann, An optimum enthalpy approach for melting and solidification with volume change. *Energies* **12**, 868 (2019).
43. S. Chen, Y. Y. Yan, W. Gong, A simple Lattice-Boltzmann model for conjugate heat transfer research. *Int. J. Heat Mass Tran.* **107**, 862–870 (2017).
44. B. Gebhart, J. C. Mollendorf, A new density relation for pure and saline water. *Deep Sea Res. Part II Top. Stud. Oceanogr.* **24**, 831–848 (1977).
45. A. Pellew, R. V. Southwell, On maintained convective motion in a fluid heated from below. *Proc. R. Soc. Lond. Math. Phys. Sci.* **176**, 312–343 (1940).
46. M. Dominguez-Lerma, G. Ahlers, D. S. Cannell, Marginal stability curve and linear growth rate for rotating Couette–Taylor flow and Rayleigh-Bénard convection. *Phys. Fluid.* **27**, 856–860 (1984).
47. E. Bodenschatz, W. Pesch, G. Ahlers, Recent developments in Rayleigh-Bénard convection. *Annu. Rev. Fluid. Mech.* **32**, 709–778 (2000).
48. W. Jenkins, "6.08 - tracers of ocean mixing" in *Treatise on Geochemistry*, H. D. Holland, K. K. Turekian, Eds. (Pergamon, Oxford, UK, 2003), pp. 223–246.
49. Z. Wang, V. Mathai, C. Sun, Self-sustained biphasic catalytic particle turbulence. *Nat. Commun.* **10**, 3333 (2019).
50. E. P. van der Poel, R. J. A. M. Stevens, D. Lohse, Comparison between two- and three-dimensional Rayleigh-Bénard convection. *J. Fluid Mech.* **736**, 177–194 (2013).
51. V. Alexiades, A. D. Solomon, Mathematical modeling of melting and freezing processes. *J. Sol. Energy Eng.* **115**, 121 (1993).